Phase behavior and characterization of heptamethyltrisiloxane-based de Vries smectic liquid crystal by electro-optics, x rays, and dielectric spectroscopy

S. P. Sreenilayam,[1] D. M. Agra-Kooijman,[2] V. P. Panov,[1] V. Swaminathan,[1] J. K. Vij,[1,*] Yu. P. Panarin,[1,3] A. Kocot,[4] A. Panov,[5] D. Rodriguez-Lojo,[5] P. J. Stevenson,[5] Michael R. Fisch,[6] and Satyendra Kumar[2,7]

[1]*Department of Electronic and Electrical Engineering, Trinity College, The University of Dublin, Dublin 2, Ireland*

[2]*Department of Physics, Kent State University, Kent, Ohio 44242, USA*

[3]*School of Electrical and Electronic Engineering, Dublin Institute of Technology, Dublin 8, Ireland*

[4]*Institute of Physics, Silesian University, Katowice 40-007, Poland*

[5]*School of Chemistry and Chemical Engineering, Queens University, Belfast, BT7 1NN, United Kingdom*

[6]*College of Applied Engineering Sustainability and Technology, Kent State University, Kent, Ohio 44242, USA*

[7]*Division of Research and Department of Physics, University at Albany, Albany, New York 12222, USA*

(Received 8 November 2016; revised manuscript received 12 January 2017; published 10 March 2017)

A heptamethyltrisiloxane liquid crystal (LC) exhibiting I–SmA^*–SmC^* phases has been characterized by calorimetry, polarizing microscopy, x-ray diffraction, electro-optics, and dielectric spectroscopy. Observations of a large electroclinic effect, a large increase in the birefringence (Δn) with electric field, a low shrinkage in the layer thickness ($\sim$1.75%) at 20 °C below the SmA^*–SmC^* transition, and low values of the reduction factor ($\sim$0.40) suggest that the SmA^* phase in this material is of the de Vries type. The reduction factor is a measure of the layer shrinkage in the SmC^* phase and it should be zero for an ideal de Vries. Moreover, a decrease in the magnitude of Δn with decreasing temperature indicates the presence of the temperature-dependent tilt angle in the SmA^* phase. The electro-optic behavior is explained by the generalized Langevin-Debye model as given by Shen *et al.* [Y. Shen *et al.*, Phys. Rev. E **88**, 062504 (2013)]. The soft-mode dielectric relaxation strength shows a critical behavior when the system goes from the SmA^* to the SmC^* phase.

DOI: 10.1103/PhysRevE.95.032701

I. INTRODUCTION

In liquid crystalline (LC) compounds, the phase transition from the orthogonal (SmA) to tilted (SmC) smectic phases is associated with an appearance of tilt (θ) between the molecular long axis n and layer normal z [Fig. 1(a)]. Due to this tilt, the layer spacing in the SmC phase (d_C) is smaller than in SmA (d_A). In the realm where the rigid-rod molecular model is valid [Fig. 1(a)], the smectic layer thickness d_C is reduced from d_A by cosθ [1–3]. In conventional SmC LCs, θ varies from 0 ° to $\sim$30 ° depending on temperature. The large layer contraction in ferroelectric SmC^* induces chevron structures which in turn result in zigzag defects [4]. These defects present a roadblock to a successful commercialization of the ferroelectric LC (FLC) devices. The FLC devices intrinsically have faster switching modes [5] than their nematic counterparts that are currently predominantly used in the industry. The objective is therefore to eliminate these zigzag defects by making the smectic layer thickness almost independent of temperature so as to have the most desirable features of FLCs in the next generation of displays.

In 1972, Diele *et al.* reported a nonchiral LC with the same layer spacing in the SmC and SmA [6]. To explain it, de Vries proposed a new type of SmA phase where the molecules are tilted as in SmC with two possible structures. In one case [7,8], SmC-like layers are stacked in a random fashion. In other words, tilt directions with the same tilt angle in different layers are randomly oriented. This implies that the azimuthal angle (φ) varies randomly from one layer to the next. No long range correlations in the azimuthal angle of the smectic layers were proposed to exist in this case. In the second model of de Vries [9], the molecules are tilted and the correlation in the tilt direction exists within a single layer, too; i.e., φ has a finite-correlation length. If the correlation length is much smaller than the wavelength of the visible light, then the phase in optical experiments should behave as "a uniaxial SmA". The results of both de Vries models should be that the directors in the SmA phase would be distributed onto a cone as shown in Fig. 1(b).

The chiral de Vries materials show electro-optic behavior due to the field-induced azimuthal reorientation of the molecules on the cone and the apparent tilt angle measured by an optical experiment in SmA thus increases with the field. They exhibit a significantly large electroclinic effect due to the azimuthal reorientation and the induced tilt gets saturated at "high" electric fields once the degeneracy in the azimuthal angle is lost (the azimuthal angle is condensed to values within narrow limits). For the zero external field, the maximum of the molecular orientational distribution function is at the cone angle (volcano distribution) rather than at the layer normal. The de Vries behavior can be described by the reduction factor defined as $R = \frac{\delta(T)}{\theta_{\mathrm{opt}(T)}} = \cos^{-1}[d_C(T)/d_{AC}]/\theta_{\mathrm{opt}}(T)$, where $\delta(T)$ is the tilt angle for the layer shrinkage relative to layer thickness d_{AC} at the smectic-A to smectic-C transition and θ_{opt} is the optical tilt angle determined by the polarizing optical microscopy [10,11]. An ideal de Vries material producing defect-free bookshelf geometry in the SmC^* phase will have the reduction factor $R = 0$.

Several research groups reported de Vries type behavior in smectic LCs composed of nonchiral [12–14] and chiral [15–19] molecules. LC materials that behave as "good de

*Corresponding author: jvij@tcd.ie

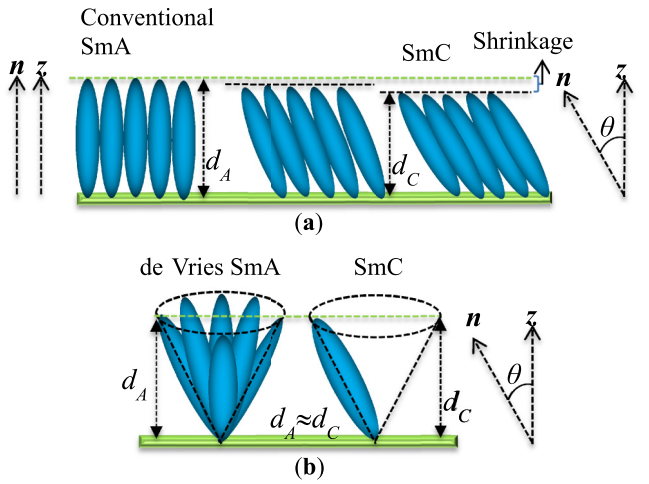

FIG. 1. Schematic representation of (a) conventional Sm*A*–Sm*C* (rigid-rod model) and (b) de Vries Sm*A*–Sm*C* (diffuse-cone model) phase transition. Here, z is the layer normal; n is the molecular long axis orientation; θ is the angle between n and z; d_C and d_A are the layer spacings in Sm*C* and Sm*A* phases, respectively.

Vries–like" so far are the siloxane-terminated TSiKN65 compound [20], its carbosilane-terminated analog W599 [21], and the 2-phenylpyrimidine derivative 8422[2F3] [22]. For these materials, the layer contraction at the smectic–A^* to smectic–C^* transition lies in the range of 0.65%–1%. In this paper, we present experimental results on the calorimetric, optical, polarization measurements, dielectric spectroscopy, and x-ray diffraction on the heptamethyl-trisiloxane derivative MSi_3MR11, which exhibits a strong electroclinic effect with birefringence strongly increasing at the SmA^*–SmC^* phase transition. Experimental results suggest that the SmA^* phase in this material is of de Vries type. The reduction factor for this material is found to be ∼0.40 20 °C below the SmA^*–SmC^* transition temperature. The electro-optic response and the induced polarization are found to be in agreement with the generalized Langevin-Debye model. The soft-mode relaxation strength of de Vries type SmA^* phase as a function of temperature exhibits critical nature when the system undergoes a transition to SmC^* phase.

II. EXPERIMENT

The molecular structure and the transition temperatures of the MSi_3MR11 are shown in Fig. 2(a). This compound was resynthesized and it has two chiral centers. The synthetic procedure is given in the Appendix. One of the objectives here is to see whether two chiral centers give rise to a similar phenomenon as compounds with one chiral center. The mesogenic core of MR11 consists of a biphenyl 2-chloro-3-methylpentanoate unit. Here "M (monosubstituted)" stands for the number of siloxane end groups attached to the mesogen MR11. The mesogen MR11 with 11 methylene units is attached to a trisiloxane backbone. The purity of the sample was found to be much higher through its analysis by nuclear magnetic resonance (NMR) than for the previously synthesized sample [23]. An analysis for the purity of the sample is also given in the Appendix. The transition

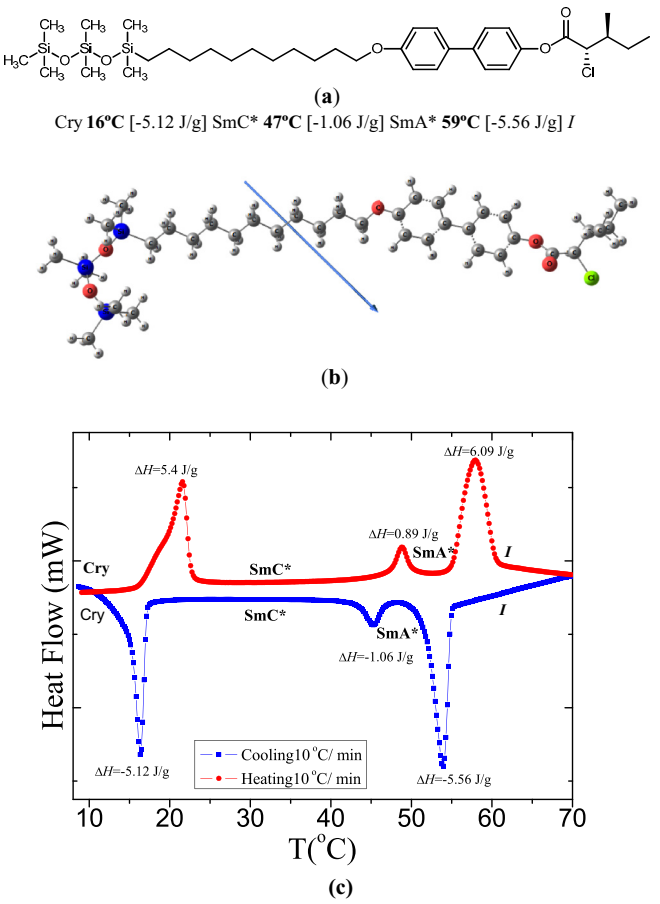

FIG. 2. (a) Molecular structure of the LC material MSi_3MR11, phase sequences, and the transition temperatures (°C) with enthalpies (J/g, in square brackets). (b) Optimized molecular geometry of MSi_3MR11. The arrow in Fig. 1(b) shows the direction of the molecular dipole moment (3.562 D). (c) DSC cooling and heating curves obtained at the rate of 10 °C min^{-1}. The transition temperatures are obtained from the cooling cycle under the quasiequilibrium condition at a rate of ∼1°C min^{-1} using polarizing microscopy. I = isotropic state, Cry = crystalline state.

temperatures [Fig. 2(a)] are obtained on cooling under a quasi equilibrium condition with a cooling rate of ∼1 °C min^{-1} using polarizing microscopy.

The optimized geometry of MSi_3MR11 [shown in Fig. 2(b)] is obtained by density functional theory (DFT) using the B3LYP method with a 6–31G (d, p) level basis set. Optimized geometry computations were carried out using the GAUSSIAN 09 software package [24]. The differential scanning calorimetry (DSC) thermograms obtained for MSi_3MR11 are shown in Fig. 2(c). In both heating and cooling cycles, this material exhibits three transition peaks. The peaks in the DSC correspond to the phase transitions I–SmA^*, SmA^*–SmC^* and the crystalline state. These phases are additionally characterized by polarizing optical microscopy. During the cooling cycle, enthalpy of the phase transition I–SmA^* is −5.56 J/g, whereas that of SmA^*–SmC^* is −1.06 J/g. The enthalpies associated with the transition temperatures (first cooling and second heating rates of 10 °C min^{-1}) show that the SmA^*–SmC^* phase transition is weakly of the first order [8,25].

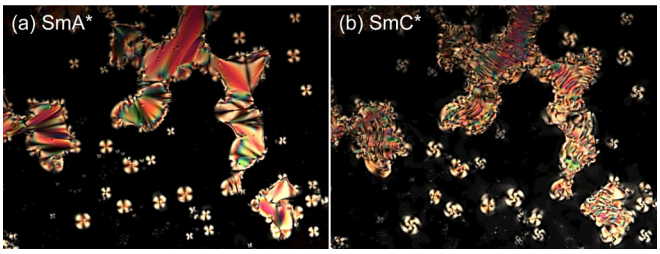

FIG. 3. Optical textures of MSi_3MR11 in (a) SmA^*, 5 °C above the SmA–SmC^* transition, T_{AC}, and (b) SmC^* (0.4 °C below T_{AC}), phases. The dark regions in the texture correspond to homeotropically aligned LC molecules.

The representative optical textures in the SmA^* and SmC^* phases (Fig. 3) were recorded using a polarizing optical microscope (Olympus BX51) equipped with a charge-coupled device (CCD) camera (SPOT, Diagnostic Instruments, Inc.) on a nonoriented sample prepared between a glass slide and cover slip placed in a Mettler Hot Stage (FP82HT) with a thermal stability of ±0.1 °C.

The x-ray diffraction study was performed on a sample contained in a flame sealed 1.0-mm quartz capillary and placed inside a Linkam hot stage (HFSX350-CAP) with a 0.05 K precision temperature controller (T95-HS) for a definitive identification of the smectic phases and for temperature dependence studies of the structure parameters such as the layer spacing, tilt angle, and the orientational order parameters. The x-ray diffraction measurements were performed using a microfocus Rigaku Screen Machine (copper anode, $\lambda = 1.542$ Å) and the diffraction patterns recorded by a Mercury 3 CCD detector of resolution 1024 × 1024 pixels (size: $73.2 \times 73.2\ \mu m^2$) placed ∼73 mm from the sample. The data were calibrated against silver behenate standards traceable to the National Institute of Standards and Technology. Data analyses were carried out using FIT2D software [26] and *Mathematica* on the background corrected data (i.e., scattering from an empty capillary was subtracted from the measured scattering data).

Electro-optic studies were made on planar cells filled with the material under study. The planar alignment in this cell is achieved by coating the indium tin oxide glass substrates with a RN1175 polymer alignment layer (Nissan Chemicals, Japan) and baking the substrates at a temperature of 250 °C for 30 min. The gap between the substrates is controlled by Mylar spacers and the actual cell thickness is measured by the technique based on the optical interference of reflected beams of light from the inner faces of the substrates of the cell. The phases are characterized by using a polarizing optical microscope (Olympus BX 52) fitted with a hot stage connected to a temperature controller (Eurotherm 2604). The electro-optic behavior of the different phases is investigated by applying ac voltages of different amplitudes from a signal generator (Agilent 33120A) amplified by a high-voltage amplifier (TReK PZD700). Dielectric spectroscopy over a frequency varying from 1 Hz to 10 MHz is carried out using a broadband Alpha High-Resolution Dielectric Analyzer (Novocontrol GmbH, Germany) under the application of a weak electric field of ($0.1\ V_{rms}$) applied across the cell with brass electrodes.

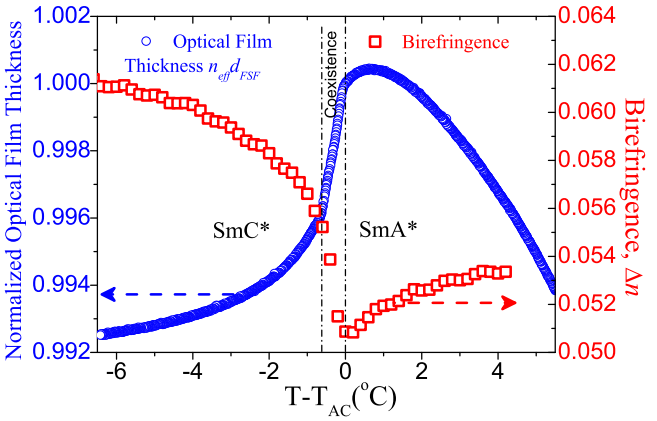

FIG. 4. Temperature dependence of the normalized optical film thickness, plotted as circles. Birefringence as squares, plotted as a function of temperature on the right-hand side. Measurements of the birefringence are carried out in the absence of external field on a 3-μm planar cell under cooling from the isotropic state. The coexistence region shown by two vertical dotted lines, where the two phases coexist, is the signature of the first-order phase SmA^*–SmC^* phase transition. In this narrow temperature range, if all the layers were to be in the SmC^* alone, the optical film thickness would have shown a small linear drop-off with temperature.

Temperature of the LC sample filled in the cell of gold coated brass electrodes is stabilized to ±0.05 °C. The dielectric spectra are recorded during the cooling process from the isotropic state.

III. RESULTS AND DISCUSSIONS

A. Freestanding film thickness birefringence and apparent tilt angle measurements

The temperature dependence of the thickness of a free-standing film (FSF) was studied using a high-resolution interferometric measurement technique [27]. A good quality homeotropic alignment of LC molecules is achieved in the FSF of MSi_3MR11; the layer thickness covers ∼10 000 layers. An experimental measurement is carried out by shining an unpolarized beam of light along the layer normal. Both heating and cooling cycles of the sample were carried out with rates as low as 0.01 °C/min in order to avoid the change in the thickness that would occur by a possible destruction of a few layers of the sample when the heating and cooling rates were large enough. Figure 4 shows temperature dependence of the optical film thickness normalized to the thickness at the SmA–SmC phase transition for the compound under study. The optical film thickness is defined as its mechanical thickness multiplied by its effective refractive index. The thickness is measured with a high-resolution interferometric technique to an accuracy better than 0.01%. If one simulates the refractive index with a change in the tilt angle, then the normalized or the relative layer thickness can be obtained. Below the isotropic temperature, the film thickness initially increases linearly but with a reduction in temperature [28] and on approaching the SmA^*–SmC^* transition, the film thickness reverses its trend from increasing to decreasing with a reduction in temperature

due to an onset of the tilt. This trend characterizes the SmA^*–SmC^* transition. For $(T–T_{AC})$ varying from 0 °C to −0.61 °C, as seen in Fig. 4, a change in the normalized film thickness shows a sharp decrease with a large drop-off in thickness. This anomalous drop is the characteristic evidence for the first-order SmA^*–SmC^* phase transition, labeled in Fig. 4 as the region where SmA^* and SmC^* coexist. If all the layers in this narrow temperature range were to be in the SmC^* alone, the optical film thickness would have exhibited rather a linear low slope drop-off with temperature, contrary to what is observed here. As already stated, the first-order behavior is additionally corroborated by the DSC observations at the SmA^*–SmC^* transition [Fig. 2(c)], which shows it to be a weak first-order transition. On further cooling of the film in the SmC^* phase, its thickness continues to decrease only relatively slightly due to an increase in the tilt angle. Finally the layer thickness reaches $d_C \approx 0.9925 d_{AC}$ at 6.3 °C below T_{AC}. In this material, the layer shrinkage of 0.75% is found to be close to the reported values of 0.73% and 0.65% for the other known de Vries materials: W599 [21] and TSiKN65 [20], respectively. This small layer shrinkage is due to an increase in the tilt angle with a reduction in temperature; it is small because in going from SmA^* to SmC^*, the in-layer directors with azimuthal angles degenerated and distributed onto a cone in SmA^* condense onto the azimuthal angles lying within narrower limits of the tilt in the SmC^* phase [see Fig. 1(b)]; this process on its own requires no change in the layer thickness.

Figure 4 also shows the plots of the apparent birefringence Δn and the optical layer thickness as a function of $(T–T_{AC})$.The magnitude of Δn first decreases on cooling and then starts to increase after the SmA^*–SmC^* phase transition has occurred [29]. The decrease in Δn is due to the de Vries tilt appearing in the SmA^* phase where the in-layer directors are distributed on the cone. Values of the birefringence, Δn, and the apparent optical tilt angle, θ_{App}, are determined by recording the intensity of transmitted beam of light through the LC sample for varying positions of polarizer and analyzer using a procedure similar to that described by Park *et al.* [30]. Experiments were conducted by applying a triangular signal of frequency 46 Hz and an amplitude of 16 $V_{0\text{-pk}}/\mu$m. The frequency is so chosen as to allow sufficient time for switching to occur while avoiding the ionic conductivity from contributing to the switching current, and different from the mains frequency of 50 Hz to avoid interference from electrical noise to the output signal. Amplitude of the voltage applied should be large enough to saturate the tilt angle but at the same time it should be much lower than the dielectric breakdown of the sample by the electric field.

The field-induced tilt angle θ_{App} and Δn values for selected temperatures close to the SmA^*–SmC^* transition are plotted as a function of the applied field in Fig. 5. Magnitude of Δn increases with electric field [Fig. 5(a)] due to the lifting of degeneracy in azimuthal angle with the field. The behavior is typical of the diffuse-cone class of models for the SmA^* phase. The tilt angle increases by the conventional electroclinic effect first and then finally it gets saturated with the field. This saturation in the tilt angle occurs in both SmC^* and in the temperature range of SmA^* closer to the SmA^*–SmC^* transition. At higher temperatures in the SmA^* phase, the electroclinic effect itself is small and

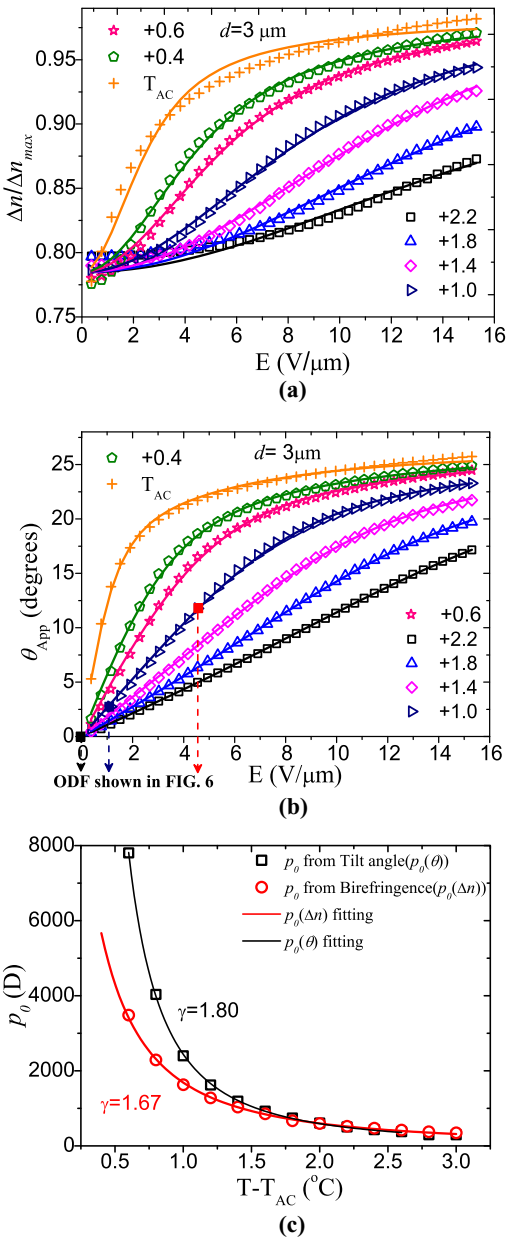

FIG. 5. (a) Measured values of the birefringence as a function of the electric field are fitted to the generalized Langevin-Debye model (solid lines) [21]; (b) the field-induced optical tilt (experimental values in symbols) are fitted to this model (solid lines). Data points for the orientational distribution function (ODF) shown in Fig. 6 are marked here in (b). (c) The local dipole moment p_0 obtained from Δn and θ_{App} fits plotted as a function of the reduced temperature. The solid lines are the best fits to the power law equation for the total dipole moment $p_0(T) = A/(T–T_{AC})^{\gamma}$; γ is the power law exponent. The divergence of $p_0(D)$ at $T = T_{AC}$ is a clear evidence of de Vries nature of the SmA phase.

hence the electric fields applied are not large enough for the saturation in θ_{App} to show up; here θ_{App} shows almost linear response to the applied electric field [31] up to the value of $\theta_{\mathrm{App}} \sim 15^\circ$. For temperatures closer to the SmC^*–SmA^* transition temperature, θ_{App} slightly deviates from the linear dependence on moderate values of the field, thus having a positive value of the second derivative with field. For large

values of the electric field, $\theta_{\rm App}$ continues to grow slowly and its second derivative becomes negative. Since the sigmoidal response of $\theta_{\rm App}(E)$ and $\Delta n(E)$ could not be satisfactorily explained by Fukuda's Langevin-Debye approach [32], Shen *et al.* [21] proposed a modified model where they added an additional term involving the square of the electric field in the expression for the free energy.

In spite of the several approaches [32–36] that exist for modeling the unusual electro-optic characteristics of the de Vries compounds, we choose the generalized Langevin-Debye model that was recently proposed by Shen *et al.* [21] for the better analysis of our data for the reasons given above. Fit of the data to the model leads to the orientational distribution function (ODF), with a complete azimuthal degree of freedom, but the tilt θ is allowed to vary by the applied field within a certain range of values. A quadratic term in the electric field in the expression of free energy has been found to have significantly improved the fit of the experimental data to the model. According to this model the free energy, U, is expressed as

$$U = -\boldsymbol{p}\left(1+\alpha\frac{\boldsymbol{p}}{|\boldsymbol{p}|}\cdot\boldsymbol{E}\right)\cdot\boldsymbol{E} = -p_0 E\sin\theta\ \cos\varphi\ (1+\alpha E\cos\varphi). \quad (1)$$

Here $p = p_0\sin\theta$ is the dipole moment of the domain correlated in the tilt brought about by the condensation of the azimuthal angle. The first term $(-p_0\,E\sin\theta\,\cos\varphi)$ given in Eq. (1) describes the dipole interaction energy and the second term $(-p_0E^2\sin\theta\cos^2\varphi)$ includes the tilt susceptibility that increases with the square of the electric field. This term leads to the sigmoidal response in both Δn and $\theta_{\rm App}$ with applied field. α is the phenomenological scaling factor. The apparent tilt angle $\theta_{\rm App}$ and the birefringence Δn as functions of the applied field become

$$\tan 2\theta_{\rm App} = \frac{\langle\sin 2\theta\cos\varphi\rangle}{\langle\cos^2\theta-\sin^2\theta\cos^2\varphi\rangle}, \quad (2)$$

$$\frac{\Delta n}{\Delta n_{\rm max}} = \frac{\langle\cos^2\theta-\sin^2\theta\cos^2\varphi\rangle}{\cos 2\theta_{\rm App}}. \quad (3)$$

An average $\langle Y\rangle$ is estimated over the orientational distribution of molecules according to the formula $\langle Y\rangle = \int_{\theta_{\rm min}}^{\theta_{\rm max}}\int_0^{2\pi} Y(\theta,\varphi)f(\theta,\varphi)\sin\theta d\theta d\varphi$, where the mean field orientational distribution function $f(\theta,\varphi)$ is expressed as $f(\theta,\varphi) = \exp[-U/k_BT]/\int_{\theta_{\rm min}}^{\theta_{\rm max}}\int_0^{2\pi}\exp[-U/k_BT]\sin\theta d\theta d\varphi$ [21]. In this model, the field-induced angle varies between the values inferred from the birefringence at zero electric field ($\theta_{\rm min}$) to the maximum field ($\theta_{\rm max}$). For the latter Δn is assumed to be saturated by the field. Here, for MSi_3MR11, the limiting values of the induced angle are found to be $\theta_{\rm min} = 16.93^\circ$ and $\theta_{\rm max} = 26.63^\circ$ [Figs. 5(a) and 5(b)]. These limiting values of θ themselves are temperature independent but the actual value within these limits is nevertheless temperature dependent. Datasets obtained for both $\Delta n(E)$ and $\theta_{\rm App}(E)$ are fitted to the model [21]. However, in contrast to the procedure used in [21], the fitting is carried out separately for both $\Delta n(E)$ and $\theta_{\rm App}(E)$. Though better fits for both (a) and (b) are obtained in each case, however, the fits with different power law exponents do reveal shortcomings of the model. Nevertheless both exponents are in the "de Vries range" and the ODF is clearly "diffuse cone". If such a limitation is material independent then this issue needs to be addressed in the future.

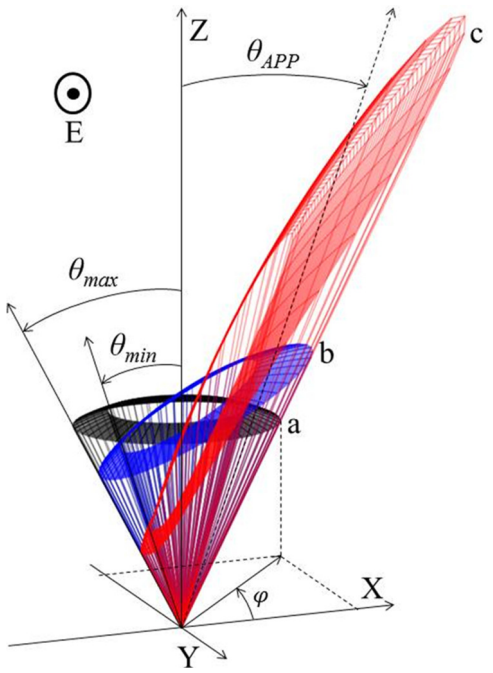

FIG. 6. The orientation distribution function $f(\theta,\varphi)$ of MSi_3MR11 at a temperature of $T = (T_{AC}+0.8)^\circ$C for various values of electric field strengths: (a) 0 V/μm (black); (b) 1.14 V/μm (blue, slanted); (c) 4.17 V/μm (red, like a long fan). *X*-*Y* is the smectic layer plane and *Z* is directed along the layer normal. Electric field is applied (normal to the plane of the paper) along the *Y* direction which lies in the smectic layer.

Figure 6 shows the "orientation distribution function" (ODF), $f(\theta,\varphi)$, for MSi_3MR11 at a temperature of $T = (T_{AC}+0.8)^\circ$C for different strengths of the electric field. The simulated ODF is rather close to a corresponding result demonstrated earlier for a different material (Figs. 5(a) and 5(b) in Ref. [21]). One can see that the model enforces a clear diffuse cone distribution by confining the cone angle between the limits of $\theta_{\rm min}$ and $\theta_{\rm max}$. In this case, the redistribution of the azimuthal angles of molecules caused by the electric field generates a finite apparent optical tilt angle very close to the one found in the experiment [Fig. 5(b)]. For the higher field strengths, nearly all of the molecules are aligned along a single direction on the outer ($\theta_{\rm max}$) cone. Note that the modeled ODF shown in Fig. 6 corresponds to the aromatic core part of the molecule that exhibits birefringence in the visible range of wavelengths.

The local dipole moment p_0, [Fig. 5(c)], determined as a fitting parameter, increases with decreasing temperature in the SmA^* phase. On approaching the SmA^*–SmC^* transition from the high-temperature side, the magnitude of p_0 in the generalized Langevin-Debye model diverges corresponding to the correlation length of the tilt domain where the azimuthal angle is condensed to values within narrow limits. Here the magnitudes of p_0 obtained from the fitting of the birefringence and the tilt data are somewhat different from each other in the vicinity of the SmA^*–SmC^* transition. Also, the scaling parameter α of the electric field varies from 0.017

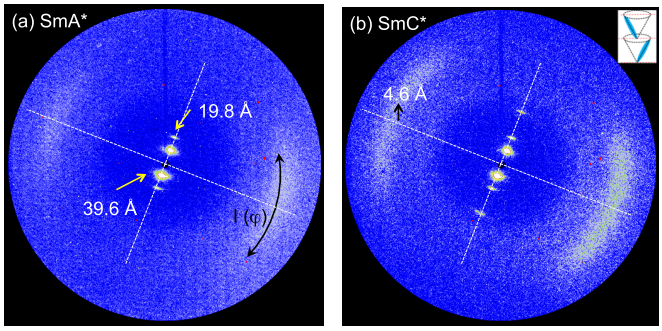

FIG. 7. Representative x-ray diffraction patterns of MSi_3MR11 in (a) SmA^* phase (1.2 °C above the T_{AC}) and (b) SmC^* phase (17.5 °C below the T_{AC}). Inset of (b) depicts the SmC^* structure.

to 0.023 μm/V for birefringence and ∼0.024 to 0.11 for data on the tilt angle. This clearly indicates that the system is more complex than the simple assumptions made in this model despite the quality of the individual fits of Δn and the apparent tilt angle to the field in the model. One of the main reasons for this discrepancy could be that the model assumes constant values of $\theta_{\min}$ and $\theta_{\max}$ independent of temperature. But measurements on the layer thickness and on temperature dependence of the zero-field birefringence reveal that $\theta_{\min}$ does at least vary with temperature. The second reason could be that the molecular biaxiality that is neglected in the model so far has to be taken into account [33].

To analyze the temperature dependence of the correlated dipole moment, p_0, we fit the data to the power law equation, $p_0(T) = A/(T-T_{AC})^{\gamma}$ [Fig. 5(c)]; γ is the power law exponent. The fit is found to be excellent but temperature dependencies of the local dipole moment are different for the birefringence and the apparent tilt angle. Exponents for Δn and θ_{App} are found to be 1.67 and 1.80, respectively. These fits lead to the conclusion that the correlated tilt (or the correlation length for azimuthal angle φ) increases with a reduction in temperature in the SmA^* phase [37] and diverges at the SmA^*–SmC^* transition; this is reminiscent of the de Vries behavior [9,18].

B. X-ray diffraction

The x-ray diffraction results for the SmA^* phase shows sharp Bragg layer reflection peaks in the small-angle region centered at ∼39.6 Å and the second-order reflection centered at ∼19.8 Å, shown in Fig. 7(a). A pair of diffuse crescents in the wide-angle region perpendicular to the layer peak located at ∼4.6 Å confirms the orthogonal smectic (SmA) nature of this phase. In the SmC^* phase [Fig. 7(b)], the third-order smectic reflections appear at ∼13.4 Å and the crescents are centered at 4.6 Å perpendicular to the layer peaks; this seems to be indistinguishable from the SmA^* phase. However, the pair of wide-angle crescents are more diffuse in the SmC^* phase than in SmA^*, where each crescent can be approximated as a sum of the two Gaussians separated by an angle 2α, α being the molecular tilt angle with respect to the layer normal. This corresponds to the domain structure with the opposite tilts, as illustrated in the inset of Fig. 7(b).

The temperature dependence of the smectic layer spacing [Fig. 8(a)], determined from the Lorentzian fits to the first small-angle peak reveals 1.75% maximum layer shrinkage in the SmC^* phase, approximately 20 ° below the smectic–A^* to smectic–C^* transition. Note that the optical layer shrinkage of 0.75% mentioned above is based on the smallest d_C spacing, obtained approximately 6 K below the SmA^*–SmC^* transition. The inset in Fig. 8(a) shows a comparison of the layer thickness measured by x-rays with the optical FSF thickness; the latter is normalized by the value at the SmA^*–SmC^* transition temperature. A different trend in

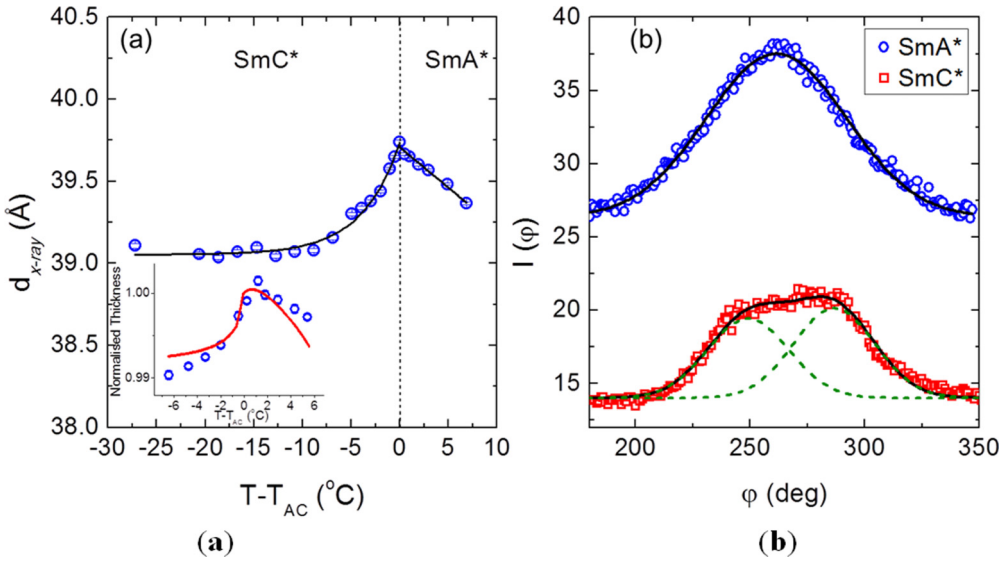

FIG. 8. (a) Temperature dependence of the layer spacing determined from the x-ray diffraction. A comparison of the results of the layer thickness from the freestanding film experiment (red solid line) and the layer thickness from the x-ray results as discrete points (circles) are given in the inset. Both curves in the inset are normalized. (b) The representative azimuthal intensity distribution $I(\varphi)$ of the wide-angle reflection centered at 4.6 Å in the SmA^* (open circles) and in the SmC^* (open squares) phases. The solid black line in SmA^* is a single Gaussian fit (FWHM = 64), while in SmC^*, it is the sum of two Gaussian fits (dashed lines) with FWHM = 36.

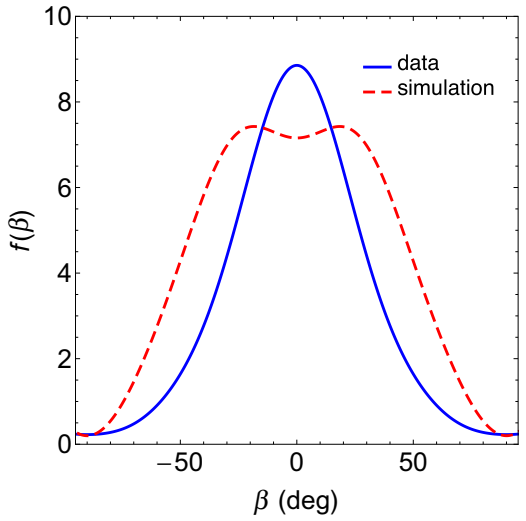

FIG. 9. The orientational distribution functions in the SmA^* phase determined from the experimentally measured $I(\varphi)$ (solid line) and the simulation (red dashed line), using molecular fluctuations $\langle\beta\rangle = 23^\circ$ and the tilt angle $\alpha = 25^\circ$.

between the two is due to a change in the refractive index tensor by the molecular tilt angle θ [27]. On cooling the cell in the SmC^* phase, this deviation reaches ~20% of the total shrinkage which can be explained by a larger value of the tilt at the phase transition as compared to the material described in [27]. The tilt angle, α, in the SmC^* phase was calculated as half the angle of separation between the centers of the two Gaussian fits to the azimuthal intensity distribution, $I(\varphi)$, of the wide-angle reflection at 4.6 Å, Fig. 8(b). Owing to the difficulty in obtaining a single domain sample, a reasonable temperature dependence of the tilt angle in the SmC^* phase specifically close to the SmA^*–SmC^* transition was difficult to determine. Nonetheless, the maximum calculated tilt angle α_{max} is ~20° in the lower SmC^* phase.

The orientational order parameter, $\langle P_2(\cos\beta)\rangle$ from the azimuthal intensity distribution $I(\varphi)$ of the wide-angle reflection centered at ~4.6 Å [Fig. 7(b)] is determined using the method of Davidson *et al.* [38]. The order parameter increases from 0.41 ± 0.01 (SmA^*) to 0.58 ± 0.01 (SmC^*). Here, β corresponds to the angle between the director and the long axis of the molecule. The low values of $\langle P_2\rangle$ obtained are the typical of the de Vries compounds with chiral components, as compared to the $\langle P_2\rangle$ for de Vries without chiral components [12,13]; however, these low values are also partly attributed to the presence of multidomains in the scanned sample volume. Correspondingly, the average molecular fluctuation [13] $\langle\beta\rangle$, decreased from 35.8° ± 0.2° (SmA^*) to 31.6° ± 0.2° (SmC^*). The extent of molecular fluctuations in the SmA^* phase is much larger than the measured maximum apparent tilt, θ_{App} ~ 25° which obscures the dip in the expected volcano-shaped ODF for de Vries compounds and makes it effectively appear as the sugarloaf distribution, shown in Fig. 9 as a solid line. To illustrate this, a simulated orientational distribution function ODF with respect to the layer normal in the de Vries SmA phase with a polar tilt angle $\alpha = 25^\circ$ and the molecular fluctuations $\langle\beta\rangle \sim 23^\circ$ is also shown in Fig. 9 (red dashed line). Note that

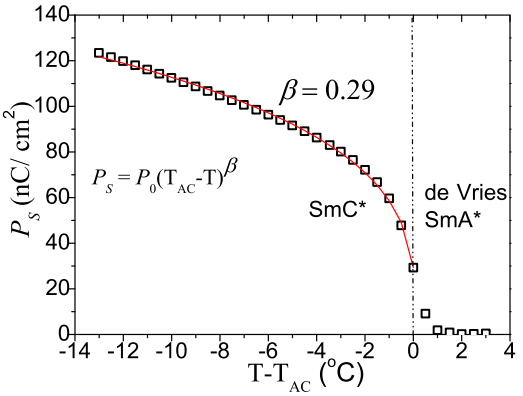

FIG. 10. Spontaneous polarization P_S vs $(T-T_{AC})$ measured on a 4-μm planar cell under cooling from the isotropic state. A triangular-waveform voltage of 50 $V_{pk\text{-}pk}$ at a frequency of 152 Hz is used in the experiment. $P_0 = 56.9\,\text{nC cm}^{-2}$. The exponent β in this figure and section III C is unrelated to earlier defined β in section III B on x-ray diffraction.

the sugarloaf-shaped ODF obtained from the x-ray experiment does not rule out the diffuse-cone distribution obtained from the optical measurements of this compound.

C. Spontaneous polarization measurement

The spontaneous polarization P_S is measured using a planar cell of thickness 4 μm as a function of temperature and the results are shown in Fig. 10. For conducting the experiment, an external triangular wave ac voltage of 50$V_{pk\text{-}pk}$ of frequency 152 Hz is applied across the planarly aligned cell using the method reported previously [39]. The measured value of P_S corresponds to its saturated value by the external field at the temperature of interest. The LC under study gives $P_S \sim 124\,\text{nC cm}^{-2}$ for a temperatiure of $T = (T_{AC}-13.5)\,^\circ\text{C}$.

P_S values are fitted to the power law equation $P_S = P_0(T_{AC}-T)^\beta$. In the fitting, it is not possible to include field-induced P_S in the SmA^* which are much higher than in a conventional SmA^* phase. The power law exponent, $\beta = 0.29$, is found from the fitting. This value so determined is close to that for the tricritical behavior; i.e., the point where the first- and second-order transitions meet with each other. The transition can then be described as "a weakly first-order transition".

D. Dielectric spectroscopy

Figure 11(a) shows the three-dimensional plot of temperature-dependent dielectric loss spectra (ε'') of a planarly aligned cell filled with MSi_3MR11. The electrodes are made up of brass; these are gold plated so as to have almost zero contact resistance. This is done to avoid the parasitic effects of the finite resistance of ITO electrodes acting in series with the cell capacitance on the dielectric spectra.

The dielectric measurements are carried out over a frequency range of 1 Hz–10 MHz using a broadband Alpha high-resolution dielectric analyser (Novocontrol GmbH, Germany), measurement made under a weak applied voltage of 0.1 V_{rms}. Temperature of the cell is controlled to within ±0.05 °C.

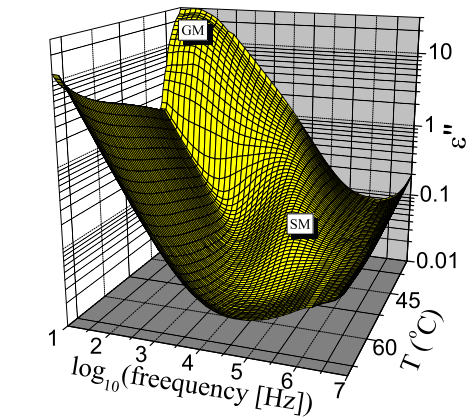

(a)

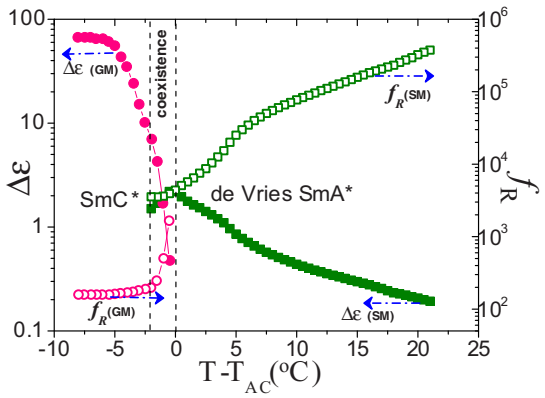

(b)

FIG. 11. (a) The three-dimensional (3D) plot of temperature-dependent dielectric loss spectra (ε'') for a 10-μm planarly aligned cell in the frequency range 1 Hz–10 MHz. The dielectric measurements are carried out on the sample under cooling from the isotropic state. Temperature is stabilized to ± 0.05 °C and the applied voltage in the experiment is fixed as 0.1 V_{rms}. (b) The dielectric relaxation strength $\Delta\varepsilon$ and the relaxation frequency f_R for both the Goldstone (GM) and soft (SM) modes are plotted as a function of the reduced temperature. The temperature range where the two phases coexist is shown by a set of vertical dotted lines close to the transition temperature.

The temperature dependencies of the dielectric strength ($\Delta\varepsilon$) and the relaxation frequency (f_R) are obtained by fitting the dielectric spectra to the Havriliak-Negami equation [40]:

$$\varepsilon^*(\omega) = \varepsilon' - i\varepsilon'' = \varepsilon_\infty + \sum_{j=1}^{n} \frac{\Delta\varepsilon_j}{[1 + (i\omega\tau_j)^{\alpha_j}]^{\beta_j}} - \frac{i\sigma_{dc}}{\varepsilon_0\omega}. \quad (4)$$

Here, ε_∞ is the high-frequency permittivity that includes the atomic and electronic polarizabilities; j is the number of relaxation processes, which varies from 1 to n; $\omega = 2\pi f$ is the angular frequency; ε_0 is the permittivity of free space; $\Delta\varepsilon_j$ refers to the dielectric relaxation strength of the jth mode. $\alpha_j (0 \ll \alpha_j \leqslant 1)$ and $\beta_j (0 \ll \beta_j \leqslant 1)$ are the symmetric and asymmetric broadening parameters of the complex dielectric function of the jth relaxation process. The $\sigma_{dc}/\varepsilon_0\omega$ is the contribution of the dc conductivity to ε''. The relaxation frequency, f_j, of the jth relaxation process is related to its relaxation time τ_j as [41]

$$f_j = \frac{1}{2\pi\tau_j}\left[\frac{\sin(\alpha_j\pi)}{2+2\beta_j}\right]^{1/\alpha_j}\left[\frac{\sin(\alpha_j\beta_j\pi)}{2+2\beta_j}\right]^{-1/\alpha_j}. \quad (5)$$

In this case we fix $j = 2$ as we focus on the two predominant modes: the Goldstone mode (GM) and the soft mode (SM), over a restricted range of frequencies, in spite of the fact that many additional modes can possibly exist in a FLC cell [42]. The dielectric spectra are analysed using the WINFIT program purchased from Novocontrol GmbH. Temperature dependenceis of the dielectric strength ($\Delta\varepsilon$) and relaxation frequency (f_R) for the two modes are shown in Fig. 11(b). On cooling the cell from the isotropic state, the amplitude of the $\Delta\varepsilon$ increases and reaches a maximum value at the SmA^*–SmC^* phase transition. The corresponding f_R decreases on cooling over a broad temperature range of the SmA^* phase but with a sharper trend in its lower-temperature range. In the studied chiral MSi_3MR11 material, the soft-mode fluctuation is dielectrically active in the SmA^* phase due to the component of the dipole moment parallel to the probe field fluctuating with the applied electric field. Remarkably strong soft-mode absorption is found in the dielectric spectra of de Vries materials over a broader temperature range in comparison to the materials that exhibit a conventional SmA phase. For example, the dielectric strength rises continuously with a reduction in temperature in this sample as opposed to a sudden rise of $\Delta\varepsilon$ in a conventional SmA phase, (compare Fig. 11(b) with Fig. 1(b) of Ref. [43] and Fig. 11(b) with Figs. 8(a) and 8(b) of [44]). Similarly the soft-mode relaxation frequency continuously decreases over a very wide temperature range in SmA^* in this sample as opposed to conventional SmA^* in which a sudden change in the frequency occurs over a very narrow range of temperatures close to the SmA^*–SmC^* transition (compare Fig. 11(b) with Fig. 1(b) of [43]) for the relaxation frequency. The soft mode normally implies fluctuations of the tilt angle. In de Vries smectic A^*, the azimuthal angle additionally also fluctuates. Hence we expect a stronger soft mode to exist in de Vries smectics than in conventional SmA^* phase. This indeed is being verified here.

IV. CONCLUSIONS

The siloxane liquid crystalline compound exhibiting the de Vries SmA^* phase was studied by DSC, polarizing optical microscopy, XRD, FSF, electro-optics, and dielectric spectroscopy. MSi_3MR11 shows a direct transition to the SmA^* phase on cooling from the isotropic state. Calorimetric studies confirm earlier works on the LC thermograms that report first-order SmA^*–SmC^* phase transition in de Vries LCs. Based on the results of Δn and θ_{App} measurements, together with the minimum layer shrinkage (~1.75%) at 20 K below SmA^*-SmC^* transition temperature obtained in this case, we characterize SmA^* of the studied material to be of the de Vries type, since an increase in the tilt angle with reducing temperature leads to a decrease in magnitude of the birefringence at zero field. An increasing Δn with applied field was found in the vicinity of the SmA^*–SmC^* transition. The generalized Langevin-Debye model as proposed by Shen *et al.* [21] is used to explain the electro-optical effects observed experimentally in the de Vries SmA^* phase of this material.

While retaining power law dependencies of the local dipole moment on temperature with slightly different exponents for birefringence and the apparent tilt angle, nevertheless the observed phenomena are well described by this model. The critical exponents indicate that the dimension of the system is greater than unity in agreement with the de Vries nature of the smectic phase. The soft-mode relaxation strength from dielectric spectroscopy shows a critical behavior when the LC system approaches the SmA^*–SmC^* phase transition. The future development of the de Vries model should include temperature dependencies of the minima and maxima of cone angles and the molecular biaxiality must be included in the model parameters. X-ray scattering gives rise to sugarloaf orientational distribution function but it does not exclude the observation of the diffuse-cone model for the electro-optical effects (birefringence and the tilt angle) as explained in the text. It would also appear that the presence of the two chiral centers in the molecule enables this material in better exhibiting the de Vries behavior.

ACKNOWLEDGMENTS

This work was supported by 13/US/I2866 from the Science Foundation of Ireland as part of the US–Ireland Research and Development Partnership program jointly administered with the United States National Science Foundation under Grant No. NSF-DMR-1410649. Financial support for the Belfast group was from the Department for Employment and Learning under with grant code USI 056. A.K. thanks National Science Centre Poland for support through Grant No. 2011/03/B/ST3/03369.

APPENDIX: SYNTHETIC PROCEDURE

Procedures for various reactions are given below in Fig. 12. All reagents were purchased from Sigma-Aldrich,

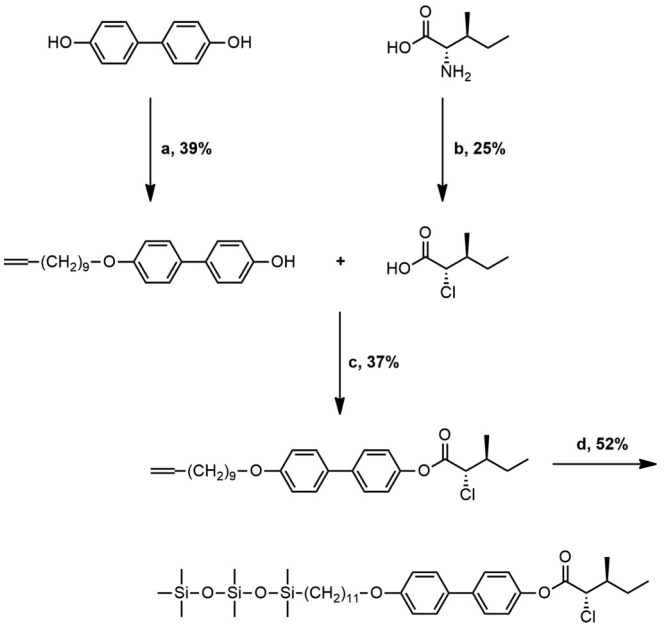

FIG. 12. Reagents and conditions: (a) 11-bromo-1-undecene, K_2CO_3, DMF; (b) $NaNO_2$, HCl, H_2O, 0 °C; (c) DMAP, DCC, THF; (d) 1,1,1,3,3,5,5-heptamethyltrisiloxane, Karstedt's catalyst, THF.

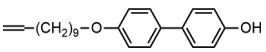

FIG. 13. Chemical Formula of compound T1.

Fluorochem, Alfa Aesar, and ABCR and used without any further purification. Solvents were purchased from Sigma-Aldrich; DMF was purchased predried and THF was dried using a sodium-benzophenone still under N_2. All reactions were generally carried out under argon using oven-dried glassware. TLC plates were performed on Merck silica gel 60 F_{254} and were visualized using a 254-nm light source. Flash column chromatography was performed on Fluorochem silica gel 60 (40–63 microns).

^{1}H and ^{13}C spectra were recorded at 25 °C ($CDCl_3$ as solvent and TMS as reference) using a Bruker 400 MHz Ultrashield (Avance 400). High resolution mass spectrometry (HRMS) spectra were recorded using a Waters TOF Electrospray Micromass LCT Premier.

The compound T1 in Fig. 13, 4′-(undec-10-en-1-yloxy)-[1,1′-biphenyl]-4-ol: 4,4′-dihydroxybiphenyl (5.00 g, 26.85 mmol), 11-bromo-1-undecene (6.26 g, 26.85 mmol) and potassium carbonate (3.72 g, 26.92 mmol) were dissolved in dry DMF (25 ml) under nitrogen and stirred at room temperature overnight. Water (25 mL) was added, the solution was neutralized with HCl (1M) and the precipitate was filtered. The solid was dissolved in hot ethanol and any insoluble particles were filtered. The suspension which formed is then filtered a second time to yield a white powder (3.40 g, 10.04 mmol, 37%).

^{1}H NMR (400 MHz, $CDCl_3$) δ: 7.45 ($d, J = 6.7$, 2H), 7.42 ($d, J = 6.6$, 2H), 6.94 ($d, J = 8.7$, 2H), 6.88 ($d, J = 8.6$, 2H), 5.82 (m, 1H), 4.98 (m, 2H), 4.72 (m, 1H), 3.98 ($t, J = 6.6$, 2H), 2.04 (m, 2H), 1.78 (m, 2H), 1.65–1.2 (m, 12H).

The compound T2 in Fig. 14, (2S,3S)-2-chloro-3-methylpentanoic acid: a suspension of L-isoleucine (5.00 g, 38.12 mmol) in 6 M HCl (40 ml) was cooled to 0 °C. The solution of sodium nitrite (2.63 g, 38.12 mmol) in water (15 ml) was added dropwise. Solution was stirred for 4 h at 0 °C and 1 h at room temperature. The compound was extracted with ethyl acetate and dried with magnesium sulfate. The solvent was evaporated and the oil distilled to give a light yellow oil (1.43 g, 9.50 mmol, 25%).

^{1}H NMR (400 MHz, $CDCl_3$) δ: 9.28 (s, 1H), 4.22 ($d, J = 6.5$, 1H), 2.10 (m, 1H), 1.65 (m, 1H), 1.34 (m, 1H), 1.05 ($d, J = 6.8$, 3H), 0.92 ($t, J = 7.4$, 3H).

The compound T3 in Fig. 15, (2S,3S)-4′-(undec-10-en-1-yloxy)-[1,1′-biphenyl]-4-yl 2-chloro-3-methylpentanoate: a solution of T1 (1.00 g, 2.95 mmol), T2 (0.44 g, 2.95 mmol), DMAP (0.04 g, 0.33 mmol), and N,N′-methanediylidenedicyclohexanamine (0.61 g, 2.96 mmol) in dry THF (30 ml) were sealed under nitrogen and stirred overnight at room temperature. The precipitate was filtered and solvent evaporated. Crude was purified using column

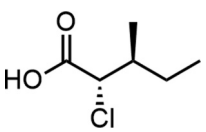

FIG. 14. Chemical Formula of compound T2.

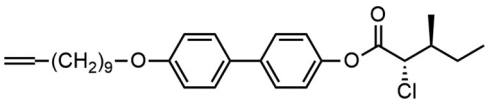

FIG. 15. Chemical Formula of compound T3.

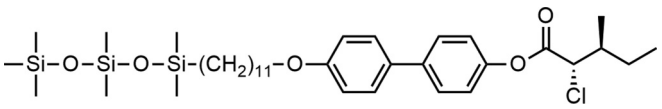

FIG. 16. Chemical Formula of compound MSi_3-MR11.

chromatography (ethyl acetate-hexane, 1:1, $R_f = 0.63$). The compound was then dissolved in hot petroleum ether and any precipitate was filtered away to give a yellow wax (0.52 g, 1.10 mmol, 37%).

^{1}H NMR (400 MHz, $CDCl_3$) δ: 7.56 ($d, J = 8.6$, 2H), 7.48 ($d, J = 8.7$, 2H), 7.16 ($d, J = 8.6$, 2H), 6.96 ($d, J = 8.7$, 2H), 5.82 (m, 1H), 4.97 (m, 2H), 4.40 ($d, J = 7.1$, 1H), 3.99 ($t, J = 6.5$, 2H), 2.24 (m, 1H), 2.05 (m, 2H), 1.80 (m, 3H), 1.70–1.16 (m, 14H), 1.15 ($d, J = 6.7$, 3H), 1.00 ($t, J = 7.4$, 3H).

The mesogen MSi_3-MR11 in Fig. 16, (2S,3S)-4′-((11-(1,1,3,3,5,5,5-heptamethyltrisiloxanyl)undecyl)oxy)-[1,1′-biphenyl]-4-yl 2-chloro-3-methylpentanoate: a solution of T3 (0.20 g, 0.42 mmol) in dry THF (10 ml) was put under nitrogen. 1,1,1,3,3,5,5-heptamethyltrisiloxane (0.14 g, 0.63 mmol) and platinum(0)-1,3-divinyl-1,1,3,3-tetramethyldisiloxane (0.021 mmol, 420 μL of 0.05 M solution) were added to the solution which was stirred for ∼4 h until the double bond was fully reduced. Solvent was evaporated and compound purified using column chromatography (DCM-Hexane, 2:8, where $R_f = 0.76$ in ethyl acetate: hexane, 1:9), to give a white wax (0.15 g, 0.22 mmol, 52%).

^{1}H NMR (400 MHz, $CDCl_3$) δ: 7.55 ($d, J = 8.8$, 2H), 7.48 ($d, J = 8.8$, 2H), 7.16 ($d, J = 8.8$, 2H), 6.96 ($d, J = 8.8$, 2H), 4.39 ($d, J = 7.1$, 1H), 3.99 ($t, J = 6.6$, 2H), 2.23 (m, 1H), 1.80 (m, 3H), 1.52–1.22 (m, 17H), 1.15 ($d, J = 6.8$, 3H), 0.99 ($t, J = 7.5$, 3H), 0.53 (m, 2H), 0.09 (s, 9H), 0.06 (s, 6H), 0.02 (s, 6H).

^{13}C NMR (101 MHz, CDCl3) δ: 168.29 (C), 159.12 (C), 149.49 (C), 139.42 (C), 132.72 (C), 128.33 (CH), 128.00 (CH), 121.58 (CH), 115.07 (CH), 68.36 (CH2), 62.88 (CH), 39.31 (CH), 33.68 (CH2), 29.87 (CH2), 29.82 (2CH2), 29.64 (CH2), 29.62 (CH2), 29.52 (CH2), 26.29 (CH2), 25.39 (CH2), 23.45 (CH2), 18.52 (CH2), 16.22 (CH3), 11.11 (CH3), 2.04 (3CH3), 1.50 (2CH3), 0.43 (2CH3).

HRMS (EI): calcd for $C_{36}H_{61}ClO_5Si_3Na$ [$M + Na^+$] 715.3413, found: 715.3438.

[1] S. Kumar, Phys. Rev. A **23**, 3207 (1981).
[2] C. R. Safinya, R. J. Birgeneau, J. D. Litster, and M. E. Neubert, Phys. Rev. Lett. **47**, 668 (1981).
[3] J. P. Lagerwall and F. Giesselmann, Chem. Phys. Chem. **7**, 20 (2006).
[4] T. P. Rieker, N. A. Clark, G. S. Smith, D. S. Parmar, E. B. Sirota, and C. R. Safinya, Phys. Rev. Lett. **59**, 2658 (1987).
[5] N. A. Clark and S. T. Lagerwall, Appl. Phys. Lett. **36**, 899 (1980).
[6] S. Diele, P. Brand, and H. Sackmann, Mol. Cryst. Liq. Cryst. **16**, 105 (1972).
[7] A. de Vries, *Abstracts Book of the 5th International Liquid Crystal Conference* (Stockholm, Sweden, 1974).
[8] A. de Vries, Mol. Cryst. Liq. Cryst. **41**, 27 (1977).
[9] A. de Vries, A. Ekachai, and N. Spielberg, Mol. Cryst. Liq. Cryst., Lett. Sect. **49**, 143 (1979).
[10] Y. Takanishi, Y. Ouchi, H. Takezoe, A. Fukuda, A. Mochizuki, and M. Nakatsuka, Jpn. J. Appl. Phys. **29**, L984 (1990).
[11] M. D. Radcliffe, M. L. Brostrom, K. A. Epstein, A. G. Rappaport, B. N. Thomas, R. Shao, and N. A. Clark, Liq. Cryst. **26**, 789 (1999).
[12] H. G. Yoon, D. M. Agra-Kooijman, K. Ayub, R. P. Lemieux, and S. Kumar, Phys. Rev. Lett. **106**, 087801 (2011).
[13] D. M. Agra-Kooijman, H. G. Yoon, S. Dey, and S. Kumar, Phys. Rev. E **89**, 032506 (2014).
[14] K. Merkel, A. Kocot, J. K. Vij, P. J. Stevenson, A. Panov, and D. Rodriguez, Appl. Phys. Lett. **108**, 243301 (2016).
[15] N. Hayashi, T. Kato, A. Fukuda, J. K. Vij, Y. P. Panarin, J. Naciri, R. Shashidhar, S. Kawada, and S. Kondoh, Phys. Rev. E **71**, 041705 (2005).
[16] C. Bahr and G. Heppke, Phys. Rev. A **41**, 4335 (1990).
[17] U. Manna, J.-K. Song, Y. P. Panarin, A. Fukuda, and J. K. Vij, Phys. Rev. E **77**, 041707 (2008).
[18] O. E. Panarina, Y. P. Panarin, J. K. Vij, M. S. Spector, and R. Shashidhar, Phys. Rev. E **67**, 051709 (2003).
[19] O. E. Panarina, Y. P. Panarin, F. Antonelli, J. K. Vij, M. Reihmann, and G. Galli, J. Mater. Chem. **16**, 842 (2006).
[20] M. S. Spector, P. A. Heiney, J. Naciri, B. T. Weslowski, D. B. Holt, and R. Shashidhar, Phys. Rev. E **61**, 1579 (2000).
[21] Y. Shen, L. Wang, R. Shao, T. Gong, C. Zhu, H. Yang, J. E. Maclennan, D. M. Walba, and N. A. Clark, Phys. Rev. E **88**, 062504 (2013).
[22] J. P. F. Lagerwall, F. Giesselmann, and M. D. Radcliffe, Phys. Rev. E **66**, 031703 (2002).
[23] G. Galli, M. Reihmann, A. Crudeli, E. Chiellini, Y. P. Panarin, J. K. Vij, C. Blanc, V. Lorman, and N. Olsson, Mol. Cryst. Liq. Cryst. **439**, 2111 (2005).
[24] M. J. Frisch *et al.*, GAUSSIAN 09, *Revision E.01* (Gaussian, Inc., Wallingford, CT, 2009).
[25] A. Mochizuki and S. Kobayashi, Mol. Cryst. Liq. Cryst. **243**, 77 (1994).
[26] A. P. Hammersley, S. O. Svensson, M. Hanfland, A. N. Fitch, and D. Hausermann, High Press. Res. **14**, 235 (1996).

[27] V. P. Panov, J. K. Vij, Y. P. Panarin, C. Blanc, V. Lorman, and J. W. Goodby, Phys. Rev. E **75**, 042701 (2007).
[28] K. L. Sandhya, Y. P. Panarin, V. P. Panov, J. K. Vij, and R. Dabrowski, Eur. Phys. J. E **27**, 397 (2008).
[29] K. Saunders, D. Hernandez, S. Pearson, and J. Toner, Phys. Rev. Lett. **98**, 197801 (2007).
[30] B. Park, S.-S. Seomun, M. Nakata, M. Takahashi, Y. Takanishi, and H. Takezoe, Jpn. J. Appl. Phys. **38**, 1474 (1999).
[31] S. Garoff and R. B. Meyer, Phys. Rev. Lett. **38**, 848 (1977); Phys. Rev. A **19**, 338 (1979).
[32] A. Fukuda, *Proceedings of the 15th International Display Research Conference of the SID* (Society for Information Display, San Jose, California, 1995), p. 61; S. Inui, N. Iimura, T. Suzuki, H. Iwane, K. Miyachi, Y. Takanishi, and A. Fukuda, J. Mater. Chem. **6**, 671 (1996).
[33] J. V. Selinger, P. J. Collings, and R. Shashidhar, Phys. Rev. E **64**, 061705 (2001).
[34] N. A. Clark, T. Bellini, R. Shao, D. Coleman, S. Bardon, D. R. Link, J. E. Maclennan, X. Chen, M. D. Wand, D. M. Walba, P. Rudquist, and S. T. Lagerwall, Appl. Phys. Lett. **80**, 4097 (2002).
[35] P. J. Collings, B. R. Ratna, and R. Shashidhar, Phys. Rev. E **67**, 021705 (2003).
[36] Z. V. Kost-Smith, P. D. Beale, N. A. Clark, and M. A. Glaser, Phys. Rev. E **87**, 050502(R) (2013).
[37] P. G. de Gennes and J. Prost, *The Physics of Liquid Crystals*, 2nd ed. (Clarendon Press, Oxford, 1993), Sec. 10.2.1, p. 527.
[38] P. Davidson, D. Petermann, and A. M. Levelut, J. Phys. II France **5**, 113 (1995).
[39] V. M. Vaksman and Y. P. Panarin, Mol. Mater. **1**, 147 (1992); V. Panov, J. K. Vij, and N. M. Shtykov, Liq. Cryst. **28**, 615 (2001).
[40] S. Havriliak, Jr. and S. Negami, Polymer **8**, 161 (1967).
[41] O. E. Kalinovskaya and J. K. Vij, J. Chem. Phys. **111**, 10979 (1999).
[42] Y. P. Panarin, H. Xu, S. T. Mac Lughadha, and J. K. Vij, Jpn. J. Appl. Phys., Part 1 **33**, 2648 (1994).
[43] H. Xu, J. K. Vij, A. Rappaport, and N. A. Clark, Phys. Rev. Lett. **79**, 249 (1997).
[44] A. Kocot, R. Wrzalik, J. K. Vij, M. Brehmer, and R. Zentel, Phys. Rev B **50**, 16346 (1994).